

# Dynamical spin phenomena generated by longitudinal elastic waves traversing $\text{CoFe}_2\text{O}_4$ films and heterostructures

Andrei V. Azovtsev and Nikolay A. Pertsev   
*Ioffe Institute, 194021, St. Petersburg, Russia*

 (Received 1 August 2019; revised manuscript received 18 November 2019; published 3 December 2019)

Electric-field control of spin dynamics in ferromagnetic films and heterostructures is crucial for the development of advanced spintronic devices with ultralow power consumption. Such control can be achieved via the magnetoelastic coupling between spins and strains created in a ferromagnet by the attached piezoelectric transducer. The efficiency of strain-mediated excitation and manipulation of spin phenomena is expected to increase drastically in materials with high magnetoelastic coefficients, such as cobalt ferrite. Here we report the state-of-the-art micromagnetic simulations of the spin dynamics arising in  $\text{CoFe}_2\text{O}_4$  films and  $\text{CoFe}_2\text{O}_4/\text{Pt}$  bilayers traversed by longitudinal elastic waves. To fully allow for the magnetoelastic coupling, we numerically solve a system of differential equations involving the Landau-Lifshitz-Gilbert equation for the magnetization and the elastodynamic equation for the mechanical displacement. The simulations show that, despite high Gilbert damping characteristic of cobalt ferrite, the injected elastic waves with frequencies around the resonance frequency of coherent magnetization precession in unstrained  $\text{CoFe}_2\text{O}_4$  film efficiently generate spin waves in this ferrimagnetic insulator. Furthermore, the generated spin wave, which has the wavelength of the driving acoustic wave, creates two secondary elastic waves due to the magnetoelastic feedback. In addition, it modifies the driving elastic wave, leading to the sound attenuation of magnetic origin with decay length about  $70 \mu\text{m}$ . In  $\text{CoFe}_2\text{O}_4/\text{Pt}$  bilayers, the magnetization precession at the interface gives rise to a spin current flowing in the Pt layer, which creates additional damping of the precession and generates a charge current via the inverse spin Hall effect. Remarkably, a circular charge flow is predicted for thick Pt layers, which leads to inhomogeneous potential distributions along their surfaces. The magnitude of the voltage between lateral sides of the Pt layer may exceed 1 nV, which can be measured experimentally.

DOI: [10.1103/PhysRevB.100.224405](https://doi.org/10.1103/PhysRevB.100.224405)

## I. INTRODUCTION

Investigations of electrically driven magnetization dynamics and spin transport in ferromagnetic heterostructures are currently at the forefront of solid-state physics because the electrical control of magnetism is of both fundamental interest and great practical importance. One of the main goals in this cutting-edge research area is the development of excitation techniques that remain efficient even at ultralow power consumption of the whole spintronic device. A promising approach to achieve this goal is based on the magnetoelastic coupling between spins and strains [1,2], which provides the opportunity to excite and control the spin dynamics with the aid of elastic strains. Combined with the ability of piezoelectrics to deform under electric fields, this feature renders possible the strain-mediated electric-field control of the magnetization dynamics and spin transport in hybrid systems comprising ferromagnetic and piezoelectric materials. Of course, efficient strain transfer between the constituents is necessary in such systems, which requires the fabrication of ferromagnetic-piezoelectric hybrids with strong interfacial mechanical coupling.

During the past decade, various types of elastic excitations have been employed in experimental studies to induce the spin dynamics in ferromagnetic heterostructures [3–18]. These excitations include bulk longitudinal sound waves injected

into a ferromagnetic film by a piezoelectric actuator [7], surface acoustic waves generated by an interdigital transducer in a piezoelectric substrate partly covered by a ferromagnetic material [5,6,10,16], and laser-induced picosecond acoustic pulses and elastic waves [3,4,11,18]. Theoretical investigations of elastically driven magnetic dynamics involve approximate analytical treatments, which employ linear approximation valid for small perturbations of the ground state [13,19–23], and micromagnetic simulations, making it possible to describe nonlinear effects [24–31]. In particular, analytical solutions have been obtained for small-angle magnetization precession driven by plane longitudinal and transverse elastic waves [21,22]. Micromagnetic simulations have been performed for ferromagnetic heterostructures excited by standing elastic waves [27] and traveling longitudinal and shear waves [28,31]. Finite-element modeling of spin waves generated by surface acoustic waves was reported as well [32].

The efficiency of strain-driven excitation of magnetic dynamics depends on the strength of magnetoelastic coupling, which for cubic ferromagnets can be described by two constants,  $B_1$  and  $B_2$ , introduced by Kittel [2] and entering the expression for the magnetoelastic free energy density  $F_{\text{mel}} = B_1[m_x^2\epsilon_{xx} + m_y^2\epsilon_{yy} + m_z^2\epsilon_{zz}] + B_2[m_x m_y \epsilon_{xy} + m_y m_z \epsilon_{yz} + m_x m_z \epsilon_{xz}]$ , where  $m_i$  and  $\epsilon_{ij}$  ( $i, j = x, y, z$ ) are the magnetization direction cosines and elastic strains, respectively. Materials with very different magnitudes

of magnetoelastic coupling constants  $B_1, B_2$  have been studied in previous works, including yttrium iron garnet ( $B_1 \approx 3 \times 10^6$  erg cm $^{-3}$ ,  $B_2 \approx 6 \times 10^6$  erg cm $^{-3}$ ) [8,22], dilute magnetic semiconductors ( $B_{1,2} < 10^8$  erg cm $^{-3}$ ) [3,4,13], nickel ( $B_{1,2} \approx 10^8$  erg cm $^{-3}$ ) [6,11,12,16,21,28,32], iron ( $B_1 \approx -3 \times 10^7$  erg cm $^{-3}$ ,  $B_2 \approx 10^8$  erg cm $^{-3}$ ) [14], Fe $_{81}$ Ga $_{19}$  alloy ( $B_{1,2} \approx -10^8$  erg cm $^{-3}$ ) [27,31], and CoFe alloys ( $B_1 \approx -3 \times 10^8$  erg cm $^{-3}$ ,  $B_2 \approx -3 \times 10^7$  erg cm $^{-3}$  for Co $_{40}$ Fe $_{60}$ ) [9,29,30]. Remarkably, even higher magnetoelastic constants  $B_1 = 5.9 \times 10^8$  erg cm $^{-3}$  and  $B_2 = -3.6 \times 10^8$  erg cm $^{-3}$  are inherent to a ferrimagnetic insulator cobalt ferrite [33]. This property makes CoFe $_2$ O $_4$  (CFO) attractive for applications in future spintronic devices exploiting strains for the excitation of spin waves and generation of spin currents. However, cobalt ferrite is also distinguished by a high Gilbert damping coefficient  $\alpha \sim 1$  [34], which raises doubts about the suitability of this ferrimagnet for such applications.

Motivated by the above considerations, we carried out micromagnetic simulations of the spin dynamics induced in CFO films and CFO/Pt bilayers by longitudinal elastic waves. Our magnetoelastic simulations are based on the numerical solution of a system of coupled differential equations comprising the Landau-Lifshitz-Gilbert (LLG) equation and the elastodynamic equation appended by magnetoelastic terms. Such a rigorous approach, implemented with the aid of homemade software, enables us to describe the coupled elastic and magnetic dynamics in ferromagnetic heterostructures [31]. In this paper, we first recall the theoretical framework of dynamical magnetoelastic phenomena and present details of our numerical calculations. Then we report results of the micromagnetic simulations performed for thick CFO films traversed by longitudinal elastic waves, which predict efficient strain-driven generation of spin waves [35] and the excitation of two additional elastic waves caused by inhomogeneous magnetization precession. Finally, spin phenomena induced by longitudinal elastic waves in CFO/Pt bilayers are described. In particular, we quantify the elastically driven magnetization precession at the CFO|Pt interface, which enables us to calculate the spin current pumped into the paramagnetic metal and the charge current flowing in Pt layer due to the inverse spin Hall effect.

## II. SIMULATIONS OF COUPLED MAGNETIC AND ELASTIC DYNAMICS

Micromagnetic simulations make it possible to predict the temporal and spatial evolution of the magnetization vector field  $\mathbf{M}(\mathbf{r}, t)$  driven by an external stimulus. Conventional simulations are restricted to the numerical solution of the LLG-type torque equation for the local magnetization  $\mathbf{M}(\mathbf{r}, t)$  in each cell of an ensemble of computational cells (see Ref. [36] and references therein). In the absence of spin-transfer torques, the standard LLG equation can be employed, which may be written as

$$\frac{d\mathbf{m}}{dt} = -\frac{\gamma}{1+\alpha^2} [\mathbf{m} \times \mathbf{H}_{\text{eff}} + \alpha \mathbf{m} \times (\mathbf{m} \times \mathbf{H}_{\text{eff}})] \quad (1)$$

if the variations of the magnetization magnitude  $|\mathbf{M}| = M_s$  are negligible, as in the case of a ferromagnet kept at a fixed temperature much lower than the Curie temperature.

Here  $\mathbf{m} = \mathbf{M}/M_s$  is the unit vector defining the magnetization direction,  $\gamma$  is the electron's gyromagnetic ratio,  $\alpha$  is the dimensionless Gilbert damping parameter, and  $\mathbf{H}_{\text{eff}}$  denotes the effective magnetic field acting on the magnetization. In the presence of strains,  $\mathbf{H}_{\text{eff}}$  includes a magnetoelastic contribution  $\mathbf{H}_{\text{mel}}$ , the account of which allows to develop an approximate description of elastically driven magnetic dynamics [26,27,29]. However, magnetization reorientations modify the strain state of the ferromagnetic material, which manifests itself in the phenomenon of magnetostriction on a macroscopic scale [2]. Therefore, the dynamical equation for the mechanical displacement  $\mathbf{u}_F(\mathbf{r}, t)$  in a ferromagnet contains additional magnetoelastic terms depending on the direction cosines of the magnetization. As a result, the rigorous treatment of dynamical magnetoelastic problems requires the solution of coupled LLG and elastodynamic equations [19,20]. This approach was employed in a few advanced micromagnetic simulations of elastically driven magnetization dynamics, which were performed recently [28,30,31].

In our simulations, the effective field  $\mathbf{H}_{\text{eff}}$  involved in Eq. (1) is evaluated as a sum of all relevant contributions, including those of the external magnetic field  $\mathbf{H}$ , exchange coupling, magnetocrystalline anisotropy, and magnetoelastic coupling. Importantly, we accurately calculate the dipolar field  $\mathbf{H}_{\text{dip}}$  [27], taking into account the variations in the dipolar interactions between differently oriented oscillating spins, which are often ignored [19–22]. The magnetoelastic contribution  $\mathbf{H}_{\text{mel}}$  is determined for ferromagnets with a cubic paramagnetic phase inherent to crystalline CFO. Introducing the Cartesian reference frame  $(x, y, z)$  with coordinate axes parallel to [100], [010], and [001] crystallographic directions of the cubic phase, we calculate the components of  $\mathbf{H}_{\text{mel}}$  from the conventional bilinear relations

$$\begin{aligned} H_x^{\text{mel}} &= -\frac{1}{M_s} [2B_1 \epsilon_{xx} m_x + B_2 (\epsilon_{xy} m_y + \epsilon_{xz} m_z)], \\ H_y^{\text{mel}} &= -\frac{1}{M_s} [2B_1 \epsilon_{yy} m_y + B_2 (\epsilon_{yx} m_x + \epsilon_{yz} m_z)], \\ H_z^{\text{mel}} &= -\frac{1}{M_s} [2B_1 \epsilon_{zz} m_z + B_2 (\epsilon_{zx} m_x + \epsilon_{zy} m_y)]. \end{aligned} \quad (2)$$

For the components of the effective field  $\mathbf{H}_{\text{mca}}$  associated with the magnetocrystalline anisotropy, we use the relations

$$\begin{aligned} H_x^{\text{mca}} &= -\frac{2}{M_s} [K_1 (m_y^2 + m_z^2) + K_2 m_y^2 m_z^2] m_x, \\ H_y^{\text{mca}} &= -\frac{2}{M_s} [K_1 (m_x^2 + m_z^2) + K_2 m_x^2 m_z^2] m_y, \\ H_z^{\text{mca}} &= -\frac{2}{M_s} [-K_u + K_1 (m_x^2 + m_y^2) + K_2 m_x^2 m_y^2] m_z, \end{aligned} \quad (3)$$

where  $K_1$  and  $K_2$  are the coefficients of fourth- and sixth-order terms in the expansion of the energy density associated with the bulk cubic anisotropy [2], and  $K_u$  defines the uniaxial magnetic anisotropy that may be present in a ferromagnetic film, which is assumed to have the (001) crystallographic orientation with surfaces orthogonal to the  $z$  axis of our reference frame (Fig. 1). Finally, the exchange field  $\mathbf{H}_{\text{ex}}$  is computed numerically using the established approach for ferromagnets as described in our previous paper [27]. Strictly

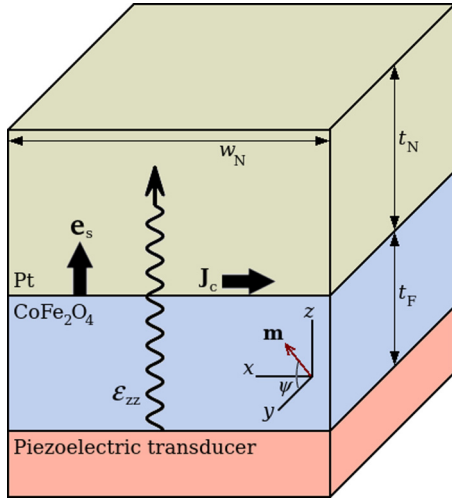


FIG. 1. Ferromagnet/normal metal heterostructure attached to a piezoelectric transducer. Longitudinal elastic wave  $\epsilon_{zz}(z, t)$  is generated by the transducer and propagates across the CFO film and Pt overlayer.  $\mathbf{e}_s$  is the direction of the spin current  $\mathbf{J}_s$  pumped into the normal metal, while  $\mathbf{J}_c$  is the density of the charge current created by  $\mathbf{J}_s$  owing to the inverse spin Hall effect.

speaking, CFO is a ferrimagnet; however, as was shown in Ref. [37], magnetic moments of the individual atoms exhibit a collinear spin structure, allowing one to treat CFO as a ferromagnet for long-wave perturbations with wavelengths much greater than the unit cell size, such as elastic waves with GHz frequencies considered in our simulations. Therefore, the exchange stiffness constant  $A_{\text{ex}}$  can be used to quantitatively describe the exchange interaction in CFO [38].

For a ferromagnet with a cubic paramagnetic phase, the elastodynamic equations of motion take the form

$$\begin{aligned}
 \rho_F \frac{\partial^2 u_x^F}{\partial t^2} &= c_{11}^F \frac{\partial^2 u_x^F}{\partial x^2} + c_{44}^F \left[ \frac{\partial^2 u_x^F}{\partial y^2} + \frac{\partial^2 u_x^F}{\partial z^2} \right] + (c_{12}^F + c_{44}^F) \\
 &\quad \times \left[ \frac{\partial^2 u_y^F}{\partial x \partial y} + \frac{\partial^2 u_z^F}{\partial x \partial z} \right] + B_1 \frac{\partial(m_x^2)}{\partial x} \\
 &\quad + B_2 \left[ \frac{\partial(m_x m_y)}{\partial y} + \frac{\partial(m_x m_z)}{\partial z} \right], \\
 \rho_F \frac{\partial^2 u_y^F}{\partial t^2} &= c_{11}^F \frac{\partial^2 u_y^F}{\partial y^2} + c_{44}^F \left[ \frac{\partial^2 u_y^F}{\partial x^2} + \frac{\partial^2 u_y^F}{\partial z^2} \right] + (c_{12}^F + c_{44}^F) \\
 &\quad \times \left[ \frac{\partial^2 u_x^F}{\partial y \partial x} + \frac{\partial^2 u_z^F}{\partial y \partial z} \right] + B_1 \frac{\partial(m_y^2)}{\partial y} \\
 &\quad + B_2 \left[ \frac{\partial(m_y m_x)}{\partial x} + \frac{\partial(m_y m_z)}{\partial z} \right], \\
 \rho_F \frac{\partial^2 u_z^F}{\partial t^2} &= c_{11}^F \frac{\partial^2 u_z^F}{\partial z^2} + c_{44}^F \left[ \frac{\partial^2 u_z^F}{\partial x^2} + \frac{\partial^2 u_z^F}{\partial y^2} \right] + (c_{12}^F + c_{44}^F) \\
 &\quad \times \left[ \frac{\partial^2 u_x^F}{\partial z \partial x} + \frac{\partial^2 u_y^F}{\partial z \partial y} \right] + B_1 \frac{\partial(m_z^2)}{\partial z} \\
 &\quad + B_2 \left[ \frac{\partial(m_z m_x)}{\partial x} + \frac{\partial(m_z m_y)}{\partial y} \right], \tag{4}
 \end{aligned}$$

where  $\rho_F$  is the volumetric mass density and  $c_{11}^F, c_{12}^F, c_{44}^F$  are the elastic stiffnesses of ferromagnetic material at constant magnetization in the Voigt notation. The system of coupled differential equations (1) and (4) is solved numerically with the aid of homemade software. It operates with a finite ensemble of computational cells characterized by their spatial positions  $\mathbf{r}$  and time-dependent vectors  $\mathbf{m}(t)$  and  $\mathbf{u}^F(t)$ . To model the excitation of a longitudinal elastic wave in a ferromagnetic film, we impose the boundary conditions  $u_x^F = u_y^F = 0$  and  $u_z^F = u_{\text{max}} \sin(2\pi \nu t)$  at the bottom film surface, which mimic the action of an attached platelike piezoelectric transducer subjected to an ac voltage (see Fig. 1). The free magnetic boundary condition  $\partial \mathbf{M} / \partial z = 0$  is used for the magnetization at both film surfaces. Since the aim of this work is to describe the effect of plane elastic waves on CFO and Pt layers with in-plane dimensions greatly exceeding their thicknesses, both  $\mathbf{M}(\mathbf{r})$  and  $\mathbf{u}^F(\mathbf{r})$  are considered independent of the coordinates  $x$  and  $y$  and allowed to vary along the  $z$  axis only. Despite this simplification, the calculations of dipolar and exchange interactions between the spins require the introduction of a three-dimensional ensemble of computation cells.

When modeling ferromagnet/normal metal bilayers, the displacement  $\mathbf{u}^N(\mathbf{r}, t)$  in a cubic normal metal with the density  $\rho_N$  and elastic stiffnesses  $c_{11}^N, c_{12}^N$ , and  $c_{44}^N$  is determined by solving numerically the standard elastodynamic equation. The free boundary condition  $\sigma_{zx}^N = \sigma_{zy}^N = \sigma_{zz}^N = 0$  is used for the upper surface of normal metal layer ( $\sigma_{ij}^N$  being the stress tensor), while proper mechanical behavior at the interface is ensured by using a unified ensemble of computational cells covering the whole bilayer. The slowing down of the magnetization precession near the interface, which is caused by the precession-induced spin pumping into adjacent normal metal [39], is taken into account via appropriate increase in the Gilbert damping parameter for computational cells adjacent to the interface.

The numerical integration of the stiff LLG equation was carried out with the aid of the projective Runge-Kutta algorithm, which employs the condition  $|\mathbf{m}| = 1$ . A finite-difference technique with midpoint derivative approximation was applied to solve the elastodynamic equations of motion for ferromagnetic film and normal metal layer. In contrast to other simulations [28], both partial differential equations were solved in their strong forms. A fixed integration step  $\delta t = 10^{-13}$  s and computational cells with the dimensions  $2 \times 2 \times 2$  nm<sup>3</sup> smaller than the exchange length  $l_{\text{ex}} = \sqrt{A_{\text{ex}} / (2\pi M_s^2)} \approx 6$  nm of crystalline CFO were used in the simulations. In this formula, saturation magnetization  $M_s$  was taken to be 425 emu cm<sup>-3</sup> [40], and we used the value of the exchange constant  $A_{\text{ex}} = 4 \times 10^{-7}$  erg cm<sup>-1</sup>, which was extracted from the fit of the magnon dispersion curve in CFO [41].

The simulations were performed for single-crystalline and amorphous CFO films and CFO/Pt bilayers. The crystalline CFO films were assumed to have the cubic magnetocrystalline anisotropy only ( $K_u = 0, K_1 = 0.9 \times 10^6$  erg cm<sup>-3</sup>,  $K_2 = 0$  [40]), whereas the uniaxial anisotropy  $K_u = 7.28 \times 10^4$  erg cm<sup>-3</sup> revealed experimentally was attributed to amorphous films ( $K_1 = K_2 = 0$ ) having  $M_s = 96$  emu cm<sup>-3</sup> [42]. The upper bound  $\alpha = 1$  of the Gilbert parameter, which is expected from the experimental data [34], was used for both films. The

elastic stiffnesses and mass densities of crystalline CFO and Pt were taken to be  $c_{11}^F = 2.57 \times 10^{12}$  dyne  $\text{cm}^{-2}$ ,  $c_{12}^F = 1.5 \times 10^{12}$  dyne  $\text{cm}^{-2}$ ,  $c_{44}^F = 0.85 \times 10^{12}$  dyne  $\text{cm}^{-2}$  [43],  $\rho_F = 5.294$  g  $\text{cm}^{-3}$  [37], and  $c_{11}^N = 3.467 \times 10^{12}$  dyne  $\text{cm}^{-2}$ ,  $c_{12}^N = 2.507 \times 10^{12}$  dyne  $\text{cm}^{-2}$ ,  $c_{44}^N = 0.765 \times 10^{12}$  dyne  $\text{cm}^{-2}$ , and  $\rho_N = 21.5$  g  $\text{cm}^{-3}$  [44]. The elastic constants of isotropic amorphous CFO were calculated by taking a Voigt-Reuss-Hill average [45] of single-crystal ones and found to be  $c_{11}^F = 2.80 \times 10^{12}$  dyne  $\text{cm}^{-2}$ ,  $c_{12}^F = 1.39 \times 10^{12}$  dyne  $\text{cm}^{-2}$ , and  $c_{44}^F = 0.71 \times 10^{12}$  dyne  $\text{cm}^{-2}$ . Then we evaluated the isotropic saturation magnetostriction using the formula  $\lambda_s = (2/5)\lambda_{100} + (3/5)\lambda_{111}$  [2,46], which enabled us to determine the magnetoelastic constants  $B_1 = B_2 = -3\lambda_s c_{44}^F = 1.32 \times 10^8$  erg  $\text{cm}^{-3}$  of the amorphous CFO with the shear modulus  $c_{44}^F$ .

Since our study is focused on spin phenomena in dynamically strained CFO films, and magnetization couples to strain rather than displacement, variations of the film magnetic response with the excitation frequency  $\nu$  were determined at a constant magnitude of the maximal strain  $\epsilon_{zz}^{\max}$  at the interface. To that end, we specified the amplitude  $u_{\max}$  of the surface displacement  $u_z^F$  by the relation  $u_{\max} = \epsilon_{zz}^{\max}/k_L$  valid for sinusoidal waves, where  $k_L = 2\pi\nu/c_L$  and  $c_L = \sqrt{c_{11}^F/\rho_F}$  are the wave number and velocity of longitudinal elastic waves, respectively. In reality, the dependence of  $u_{\max}$  on the frequency of ac voltage applied to the attached transducer is dominated by piezoelectric resonances and antiresonances. Since the resonance frequency depends on the transducer's thickness and material parameters [47], it can be tuned in a wide range. Hence, the displacement amplitude  $u_{\max}$  at a given frequency  $\nu$  can be adjusted to a desirable value even without applying high ac voltages to the piezoelectric transducer. Regarding the feasibility of displacements assumed in our simulations, the largest value of  $u_{\max}$  is of the order of  $10^{-2}$  nm for crystalline films and about 0.5 nm for amorphous ones, which is easily achievable using available piezoelectric materials [48]. Furthermore, elastic waves with frequencies much higher than the transducer's fundamental resonance frequency can be excited in the attached ferromagnet by short voltage pulses [49]. It should be noted that sub-picosecond laser pulses make it possible to generate packets of elastic waves with frequencies exceeding 100 GHz [50–52].

### III. GENERATION OF SPIN WAVES IN THICK CFO FILMS

#### A. Crystalline CFO films

To study the propagation of magnetoelastic perturbations in CFO, we performed a series of simulations of films with thicknesses much greater than the wavelength  $\lambda_L = c_L/\nu$  of the driving longitudinal elastic wave. Since such a wave can create only the component  $H_z^{\text{mel}} = -2B_1\epsilon_{zz}m_z/M_s$  of the effective magnetoelastic field  $\mathbf{H}_{\text{mel}}$ , an external magnetic field  $\mathbf{H}$  was introduced along the  $z$  axis, inducing the magnetization component  $m_z$  necessary to obtain nonzero  $H_z^{\text{mel}}$ . At the assumed field strength  $H_z = 1600$  Oe, the equilibrium magnetization direction has an elevation angle  $\psi \approx 9.9^\circ$  in the unstrained CFO film with infinite in-plane dimensions (see Fig. 1). Since the most efficient excitation of magnetization dynamics is expected near the resonance frequency  $\nu_r$  of

the coherent magnetization precession in the unstrained film [27], we first determined this frequency using two different approaches. First, an analytical formula for the ferromagnetic resonance (FMR) frequency [53] was used to calculate  $\nu_r$  under the assumption of negligible damping, yielding  $\nu_r(\alpha = 0) = 16$  GHz. Second, to accurately determine  $\nu_r$  of the CFO film characterized by the damping parameter  $\alpha = 1$ , we ran a series of simulations of the film's magnetization response to a uniform ac magnetic field  $\delta H_z \sim \sin 2\pi\nu t$ . The largest precession amplitude was registered at  $\nu = \nu_r = 11$  GHz, which is about 1.5 times smaller than the resonance frequency  $\nu_r(\alpha = 0)$ . The difference is substantial, showing that high Gilbert damping  $\alpha \sim 1$  can reduce the resonance frequency considerably. This feature can be expected from the LLG equation (1), where the damping parameter appears on the right-hand side both in the prefactor  $\gamma/(1 + \alpha^2)$  and in the second term inside the square brackets.

After determining the resonance frequency, we focused on micromagnetic simulations of CFO films subjected to a periodic surface displacement  $u_z^F(z = 0, t) = u_{\max} \sin 2\pi\nu t$  with the frequency  $\nu$  spanning a wide range around  $\nu_r = 11$  GHz and amplitudes  $u_{\max}(\nu)$  providing the maximal strain  $\epsilon_{zz}^{\max} = 5 \times 10^{-6}$  at the surface. The simulations showed that such displacement  $u_z^F(z = 0, t)$  generates a longitudinal elastic wave  $\epsilon_{zz}(z, t)$  propagating inside the film [see Fig. 2(a)]. Owing to the magnetoelastic effective field  $H_z^{\text{mel}}$  created by the strain wave, the magnetization of CFO starts to precess around its initial equilibrium direction. The magnetization precession, in turn, modifies the strain state of CFO by virtue of the magnetoelastic terms involved in Eq. (4). In the considered films with infinite dimensions in the  $xy$  plane, only components  $\epsilon_{xz}$ ,  $\epsilon_{yz}$ , and  $\epsilon_{zz}$  of the strain tensor can be affected by such magnetoelastic feedback. Concerning shear strains, the magnetization dynamics leads to the generation of transverse waves  $\epsilon_{xz}(z, t)$  and  $\epsilon_{yz}(z, t)$  shown in Fig. 2(b), where the displacements  $u_x^F$  and  $u_y^F$  are orthogonal to the wave vector  $\mathbf{k}_T$  oriented along the  $z$  axis. Such *secondary elastic waves* were not revealed in previous micromagnetic simulations of longitudinal elastic wave propagation along a Ni bar [28], but their appearance was predicted for  $\text{Fe}_{81}\text{Ga}_{19}$  films traversed by shear waves [31]. The amplitudes of secondary waves  $\epsilon_{xz}(z, t)$  and  $\epsilon_{yz}(z, t)$  are about 1000 and 200 times smaller than that of the driving longitudinal wave, and their profiles show a peculiar behavior, being different in two regions of the film indicated in Fig. 2(b). The Fourier analysis shows that, in the subsurface region  $z < z^*$ , each of the waves  $\epsilon_{xz}(z, t)$  and  $\epsilon_{yz}(z, t)$  is actually a superposition of two waves having different wavelengths. The wave with a larger amplitude (wave I) has the wavelength  $\lambda_T = c_T/\nu$  of a shear wave traveling in CFO with the velocity  $c_T = \sqrt{c_{44}^F/\rho_F}$ , while the wave II with a smaller amplitude has the wavelength  $\lambda_L = c_L/\nu$  of the driving longitudinal wave. In contrast, at distances  $z > z^*$  from the surface only the wave II having the wavelength  $\lambda_L$  propagates in the film. The simulations show that the size  $z^*$  of the subsurface region increases with time as  $z^* = c_T t$ . This result proves that the wave I is excited by the magnetization precession occurring at the surface  $z = 0$ . This “free” shear wave then travels inward CFO with its inherent velocity  $c_T$ . Since  $c_T$  is smaller than  $c_L$  ( $\approx 4$  km/s versus  $\approx 7$  km/s in crystalline CFO), the front of the wave I lags from that of the

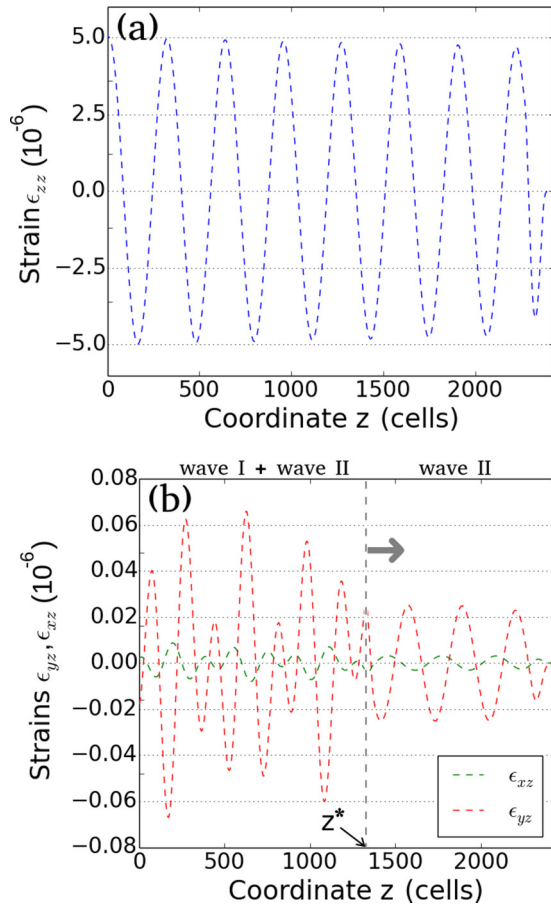


FIG. 2. Elastic waves emerging in the crystalline CFO film at the excitation frequency  $\nu = 11$  GHz. (a) Primary longitudinal wave generated by the piezoelectric transducer at the time  $t = 0.69$  ns. (b) Secondary transverse waves excited by the backaction of the magnetization precession on strain state of the film ( $t = 0.69$  ns). The film thickness equals 4848 nm, and the coordinate  $z$  is given in units of computational cell size amounting to 2 nm.

wave II, which leads to the formation of two regions shown in Fig. 2(b). Since wave II has the wavelength  $\lambda_L$  and advances with the velocity  $c_L$ , this wave is a forced shear wave excited by the inhomogeneous magnetization precession in the whole longitudinal driving wave.

The backaction of magnetization dynamics on strain  $\epsilon_{zz}(z, t)$  associated with the driving elastic wave leads to a continuous decrease of the wave amplitude  $\epsilon_{zz}^{\max}(z)$  with increasing distance  $z$  from the film surface. This decay of the driving wave, which is noticeable in Fig. 2(a), stems from the energy transfer to the magnetic subsystem induced by strong magnetoelastic coupling and from high Gilbert damping hindering the magnetization precession. Dependences  $\epsilon_{zz}^{\max}(z)$  extracted from the results of simulations performed at different excitation frequencies  $\nu$  have been successfully fitted by the exponential function  $\epsilon_{zz}^{\max}(z) \sim \exp(-z/L_{\text{dec}})$  [see Fig. 3(a)]. The decay length  $L_{\text{dec}}$  continuously decreases with increasing excitation frequency, dropping from about 750 to 50  $\mu\text{m}$  in the frequency range presented in Fig. 3(b). It should be emphasized that the revealed fading of the longitudinal strain wave has a solely magnetic origin, as no elastic damping is involved in Eq. (4). Our finding may be useful for

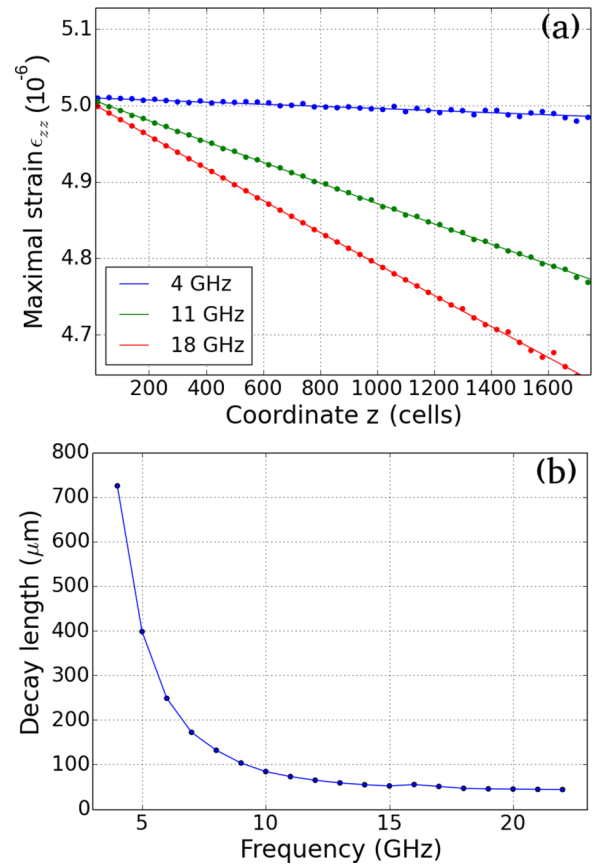


FIG. 3. Decay of the driving elastic wave in the crystalline CFO film caused by the strain-induced magnetization precession. (a) Decrease of the wave amplitude  $\epsilon_{zz}^{\max}(z)$  with increasing distance  $z$  from the film surface calculated at three different excitation frequencies. Dots show simulation results, while solid lines represent their fitting by the exponential function  $\epsilon_{zz}^{\max}(z) \sim \exp(-z/L_{\text{dec}})$ . (b) Dependence of the decay length  $L_{\text{dec}}$  on excitation frequency.

understanding the nature of sound attenuation in CFO and other materials with strong magnetoelastic coupling and high magnetic damping.

Our micromagnetic simulations also showed that the magnetization dynamics generated by the longitudinal elastic wave has the form of a spin wave evolving in the CFO film. Figure 4(a) demonstrates that the spin wave has the same wavelength, velocity, and almost sinusoidal shape as the driving strain wave. Hence, the latter serves as a carrier of the spin wave, which otherwise would decay rapidly in CFO due to high magnetic damping inherent in this ferromagnetic insulator. Importantly, the spin-wave decay length  $L_{\text{dec}}(\nu)$  follows the curve shown in Fig. 3(b), amounting to 73  $\mu\text{m}$  at  $\nu = 11$  GHz (instead of  $L_{\text{dec}} \approx 11$  nm in the case of spin wave propagating in CFO on its own). Of course, the tightly coupled pair of elastic and spin waves could be regarded as a single magnetoelastic wave as well. However, it should be emphasized that both waves obey a purely elastic dispersion relation  $k_L = 2\pi\nu/c_L$  without any detectable deviations at all studied frequencies. This absence of hybridization of elastic and spin waves, which may be due to high Gilbert damping in CFO, motivated us to avoid using the term “magnetoelastic wave” throughout the paper.

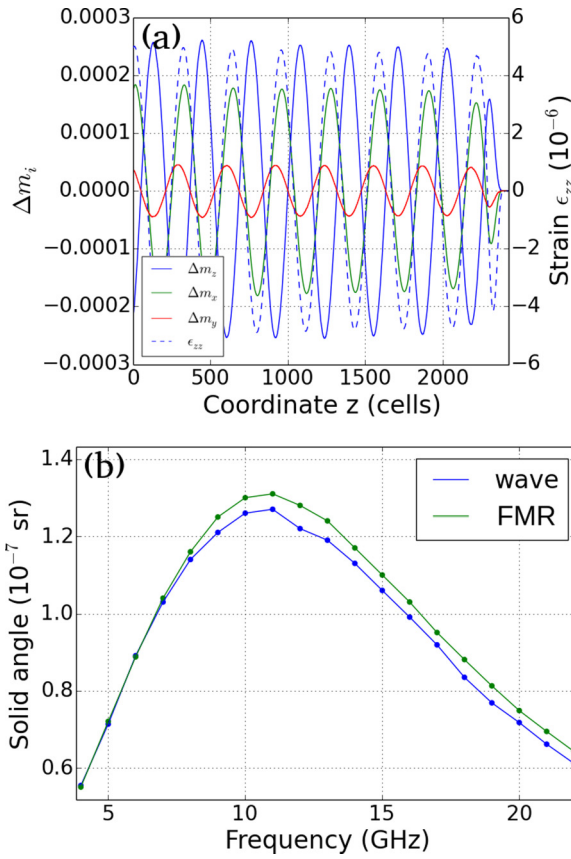


FIG. 4. Spin wave generated by the longitudinal elastic wave propagating in the crystalline CFO film. (a) Spatial distributions of the changes  $\Delta m_i$  ( $t = 0.69$  ns) in the direction cosines of oscillating magnetization at the excitation frequency  $\nu = 11$  GHz (solid lines) in comparison with those of the strain  $\epsilon_{zz}$  in the driving elastic wave (blue dashed line). (b) Frequency dependence of the maximal solid angle of magnetization precession in the spin wave at the distance  $z = 2\lambda_L$  from the film surface in comparison with that calculated for the uniform FMR mode at the ac magnetic field  $\delta H_z$  with an amplitude of 14 Oe.

To evaluate the efficiency of spin wave generation at different excitation frequencies, we determined the maximal solid angle  $\Omega$  of the magnetization precession at a representative distance  $z = 2\lambda_L$  from the film surface. Figure 4(b) compares the obtained dependence  $\Omega(\nu)$  with that of a coherent magnetization precession induced by a uniform ac magnetic field in the unstrained CFO film. Remarkably, the spin-wave amplitude becomes maximal exactly at the resonance frequency  $\nu_r = 11$  GHz of the coherent precession corresponding to a uniform FMR mode. At this frequency, the angle  $\Omega$  amounts to  $1.3 \times 10^{-7}$  sr at the low input strain  $\epsilon_{zz}^{\max} = 5 \times 10^{-6}$  employed in our simulations, which indicates significant efficiency of the acoustically driven generation of spin waves. Therefore, crystalline CFO can be regarded as a suitable material for acoustic spintronics despite its high Gilbert damping.

### B. Amorphous CFO films

Similar micromagnetic simulations have been performed for thick amorphous CFO films. Owing to comparatively strong uniaxial anisotropy overriding the shape anisotropy,

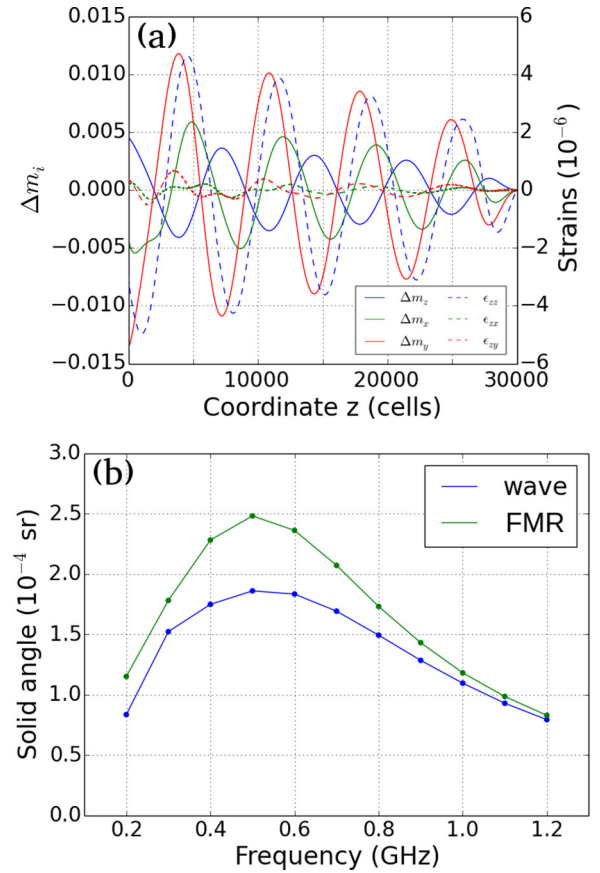


FIG. 5. Spin wave and elastic waves generated in the amorphous CFO film. (a) Spatial distributions of the changes  $\Delta m_i$  ( $t = 8.3$  ns) in the magnetization direction cosines at the excitation frequency  $\nu = 0.5$  GHz (solid lines) plotted together with the strains  $\epsilon_{zz}$ ,  $\epsilon_{xz}$ , and  $\epsilon_{yz}$  in the primary longitudinal wave and secondary transverse waves (dashed lines). (b) Frequency dependence of the maximal solid angle of magnetization precession in the spin wave at the distance  $z = 2\lambda_L$  from the film surface in comparison with that calculated for the uniform FMR mode at the ac magnetic field  $\delta H_z$  with an amplitude of 4.5 Oe.

the equilibrium magnetization direction in such films appears to be orthogonal to film surfaces. At this orientation, the magnetoelastic effective field  $\mathbf{H}_{\text{mel}}$  created by the longitudinal elastic wave does not impose any torque on the magnetization  $\mathbf{M}$  because  $H_x^{\text{mel}} = H_y^{\text{mel}} = 0$ . Therefore, a small magnetic field of 100 Oe was introduced along the  $y$  axis, tilting  $\mathbf{M}$  away from the perpendicular-to-plane orientation by about  $19^\circ$ . Since the saturation magnetization  $M_s = 96$  emu  $\text{cm}^{-3}$  of the amorphous film is rather low [42], and the uniaxial anisotropy parameter  $K_u = 7.28 \times 10^4$  erg  $\text{cm}^{-3}$  is much smaller than the cubic anisotropy coefficient  $K_1 = 9 \times 10^5$  erg  $\text{cm}^{-3}$  of the crystalline CFO, the resonance frequency  $\nu_r$  drops strongly, amounting to 0.5 GHz at  $H_y = 100$  Oe. At such value of excitation frequency, the wavelength  $\lambda_L$  of the driving longitudinal wave becomes very long ( $\lambda_L = 14.5$   $\mu\text{m}$ ), which forced us to increase the film thickness up to  $t_F = 60$   $\mu\text{m}$  to encompass several wavelengths  $\lambda_L$  in the simulations.

Figure 5 shows the results obtained at the same input strain  $\epsilon_{zz}^{\max} = 5 \times 10^{-6}$  as was used in the simulations of crystalline CFO films. We see that the magnetoelastic dynamics in the

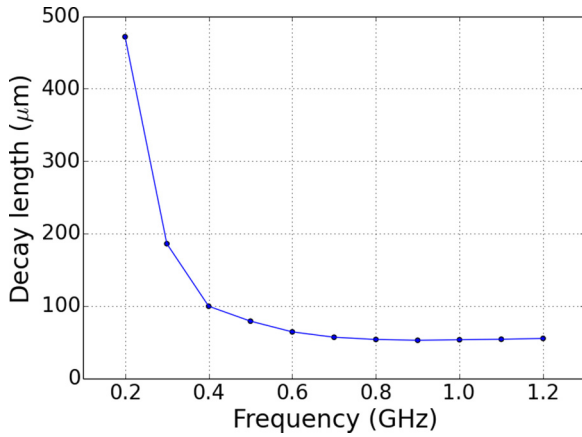


FIG. 6. Decay length of the driving elastic wave in the amorphous CFO film plotted as a function of the excitation frequency. The decay length of the elastically generated spin wave follows the same curve.

amorphous film is qualitatively similar to that in the crystalline one but significantly differs quantitatively. Like in the case of crystalline CFO, the amplitude of elastically generated spin wave reaches its maximum at the frequency  $\nu_r$ , which amounts to 0.5 GHz for the amorphous film [see Fig. 5(b)]. However, the maximal solid angle  $\Omega$  of the magnetization precession is three orders of magnitude larger than in the crystalline film ( $\approx 10^{-4}$  sr versus  $\approx 10^{-7}$  sr). Such drastic increase in the precession amplitude results from the combination of two factors. First, the magnetoelastic effective field  $H_z^{\text{mel}} = -2B_1\epsilon_{zz}m_z/M_s$  acting on the magnetization is much higher in the amorphous film, because the direction cosine  $m_z$  is much larger here (0.947 versus 0.172), while the ratio  $B_1/M_s$  is practically the same for both amorphous and crystalline CFO. Second, the contributions to the effective field  $\mathbf{H}_{\text{eff}}$  that hinder the magnetization precession are smaller in the case of amorphous film owing to much lower applied magnetic field  $\mathbf{H}$  ( $H_y = 100$  Oe versus  $H_z = 1600$  Oe) and weaker magnetocrystalline anisotropy ( $K_u \ll K_1$ ).

Much larger amplitude of the magnetization precession in the amorphous film leads to the generation of stronger secondary elastic waves, which are shown in Fig. 5(a). In contrast to the crystalline CFO film, where such shear waves are two to three orders of magnitude weaker than the driving longitudinal wave, in the amorphous film the strains  $\epsilon_{zy}^{\text{max}}$  and  $\epsilon_{zx}^{\text{max}}$  generated at  $\nu = 0.5$  GHz are only about 14 and 21 times smaller than  $\epsilon_{zz}^{\text{max}}$ , respectively. The magnetization precession also induces noticeable attenuation of the longitudinal wave, which is characterized by the frequency-dependent decay length  $L_{\text{dec}}(\nu)$  shown in Fig. 6. Remarkably,  $L_{\text{dec}}(\nu = 0.5 \text{ GHz}) \approx 79 \mu\text{m}$  is comparable to the decay length  $L_{\text{dec}}(\nu = 11 \text{ GHz}) \approx 73 \mu\text{m}$  of the longitudinal wave in the crystalline CFO film. To explain this interesting result, we first recall that the rate of energy dissipation in the magnetic subsystem is governed by the term  $\alpha \mathbf{m} \times d\mathbf{m}/dt$  in the LLG equation. Accordingly, this rate depends on the amplitude and frequency of the magnetization precession in the elastically generated spin wave. Furthermore, the magnetization precession affects the strain  $\epsilon_{zz}$  in the longitudinal elastic wave via the term  $B_1\partial(m_z^2)/\partial z$  in Eq. (4), which shows that the magnetically induced

attenuation of the elastic wave also depends on its wavelength  $\lambda_L$  and the initial magnitude of the magnetization direction cosine  $m_z$ . Since the out-of-plane precession amplitude  $\delta m_z$  and the initial direction cosine  $m_z$  are much larger in the amorphous CFO film, the decay length  $L_{\text{dec}}$  could be expected to be much bigger in such film. However, when comparing the attenuation under the resonance conditions, these differences are compensated for by the 23 times smaller wavelength  $\lambda_L$  in the crystalline CFO combined with the larger magnetoelastic coupling constant  $B_1$  of this material ( $5.9 \times 10^8 \text{ erg cc}^{-1}$  versus  $1.32 \times 10^8 \text{ erg cc}^{-1}$  in the amorphous one).

It is also interesting to evaluate the energy transfer from the driving elastic wave to the magnetic subsystem. In the steady-state regime, the amplitude of the strain-induced magnetization precession becomes constant so that the energy loss caused by the Gilbert damping fully compensates the energy transfer from the elastic wave. The dissipation rate  $dF/dt$  in the magnetic subsystem can be evaluated using the well-known relation  $dF/dt = dF/d\mathbf{m} \cdot d\mathbf{m}/dt = -M_s \mathbf{H}_{\text{eff}} \cdot d\mathbf{m}/dt$ . Using Eq. (1) to determine  $d\mathbf{m}/dt$ , after some algebra one obtains

$$\frac{dF}{dt} = -\frac{\alpha\gamma}{1+\alpha^2} M_s (\mathbf{m} \times \mathbf{H}_{\text{eff}})^2. \quad (5)$$

Since the dependences  $\mathbf{m}(t)$  and  $\mathbf{H}_{\text{eff}}(t)$  are known from the micromagnetic simulations, this relation enables us to evaluate the dissipation rate  $dF/dt$ , which quantifies the energy transferred from the elastic wave in the steady-state regime. The calculation shows that, at a representative distance  $z = 2 \mu\text{m}$  from the surface, the energy-transfer rate averaged over the period of magnetization precession amounts to  $5.64 \times 10^9 \text{ erg cc}^{-1} \text{ s}^{-1}$  in the crystalline CFO film and to  $4.65 \times 10^9 \text{ erg cc}^{-1} \text{ s}^{-1}$  in the amorphous one. The similarity of these values is consistent with similar decay lengths  $L_{\text{dec}}$  found for the crystalline and amorphous CFO films. It should also be noted that the decay lengths of the secondary elastic waves in the region  $z > z^*$  appear to be close to that of the driving longitudinal wave in both crystalline and amorphous films (at least at the resonance frequency  $\nu_r$ ). This interesting result confirms our statement that the wave II is a forced shear wave generated in the whole driving wave.

Summarizing the results obtained for the excitation of spin waves in CFO by longitudinal elastic waves, we may conclude that this technique appears to be efficient for both crystalline and amorphous CFO films despite high Gilbert damping inherent to this ferrimagnet. Using the solid angle  $\Omega_r$  of magnetization precession at the resonance frequency as a merit factor, we can compare CFO with traditional materials considered for acoustically driven spin wave generation, namely, yttrium iron garnet (YIG) and  $\text{Fe}_{81}\text{Ga}_{19}$  alloy (galfenol). From Eqs. (2) and (3), it follows that the spin-wave amplitude can be enhanced by using a magnetoelastic material with a large ratio  $B_1/M_s$  and small magnetocrystalline anisotropy factors  $K_1/M_s$  and  $K_u/M_s$ . In this respect, CFO is advantageous because it has very large ratio  $B_1/M_s \approx 1.4 \times 10^6 \text{ Oe}$ , greatly exceeding those of galfenol ( $-6.81 \times 10^4 \text{ Oe}$ ) and YIG ( $2.49 \times 10^4 \text{ Oe}$ ). However, the anisotropy factors of crystalline ( $K_1/M_s \approx 2120 \text{ Oe}$ ) and amorphous ( $K_u/M_s \approx 760 \text{ Oe}$ ) CFO films are larger than those of galfenol ( $K_1/M_s \approx 130 \text{ Oe}$ ) [31] and YIG ( $K_1/M_s \approx 43 \text{ Oe}$ ) [22]. To clarify the

situation, we performed additional magnetoelastic simulations to determine  $\Omega_r$  for  $\text{Fe}_{81}\text{Ga}_{19}$  and YIG films using available parameters of these materials [22,54,55]. It was found that, at the magnetic field  $H_z = 1600$  Oe employed in the simulations of the crystalline CFO film,  $\Omega_r$  is about  $0.8 \times 10^{-8}$  sr in  $\text{Fe}_{81}\text{Ga}_{19}$  and about  $3.5 \times 10^{-6}$  sr in YIG. Hence, crystalline CFO ( $\Omega_r \approx 1.3 \times 10^{-7}$  sr) is predicted to be more efficient than galphenol for the strain-driven excitation of spin waves, but the small anisotropy factor  $K_1/M_s$  and extremely low Gilbert damping  $\alpha = 8 \times 10^{-5}$  [55] of YIG make it unrivaled for the resonance excitation. However, the FMR linewidth is very narrow in this material, which requires fine-tuning and high stability of the excitation frequency for using this advantage in device applications. In contrast, CFO has a very broad linewidth, which renders it possible to efficiently generate the magnetization precession in a rather wide range of excitation frequencies, providing robust devices for acoustic spintronics, such as spin injectors into normal metals and semiconductors.

#### IV. GENERATION OF SPIN AND CHARGE CURRENTS IN CFO/Pt BILAYERS

Having established that longitudinal elastic waves can efficiently excite spin waves in both crystalline and amorphous CFO thick films, we proceeded to theoretical studies of spin phenomena in CFO/Pt bilayers. Our investigation involved simulations of the elastically driven magnetization dynamics in the CFO layer and calculations of spin and charge currents generated in the Pt one by the magnetization precession at the CFO|Pt interface. Simulations of the magnetoelastic phenomena occurring in the bilayers were performed as described in Sec. II for excitation frequencies of 11 and 0.5 GHz providing maximal amplitudes of the spin waves generated in the crystalline and amorphous CFO films, respectively. The thicknesses of CFO layers were set equal to one wavelength of the driving longitudinal wave, which yields  $t_F = 634$  nm for the crystalline layer and  $t_F = 14\,540$  nm for the amorphous one, because preliminary runs showed that this choice maximizes the amplitude of the magnetization precession at the CFO|Pt interface. Reflections of the primary and secondary elastic waves at this interface were fully taken into account and found to be rather small for both crystalline and amorphous films (transmittance of the driving wave is about 0.84 and 0.85, respectively). However, reflections of elastic waves from the free surface of the Pt layer were disregarded in the simulations of the CFO one, because the reflected waves would complicate the magnetoelastic dynamics greatly. At thickness  $t_N = 4 \mu\text{m}$  assumed for the Pt layer, the time  $\tau_L$  needed for the longitudinal wave to cross the CFO/Pt bilayer and return back to the CFO|Pt interface equals 2.1 ns for the crystalline film and 4 ns for the amorphous one. To get rid of reflected waves at longer simulation times  $t > \tau_L$ , we assigned an artificial elastic damping to the Pt layer, which provided a rapid decay of elastic waves in it. This was achieved by adding a term  $\beta \partial u_i^N / \partial t$  with  $\beta \cong 4.3 \times 10^{11}$  g cm $^{-3}$  s $^{-1}$  to the elastodynamic equation of motion. Such approach was validated by comparing the results of the simulations performed for CFO/Pt bilayers comprising highly damped and undamped Pt layers. It was found that at times  $t < \tau_L$  there is no significant

difference in the magnetization and elastic dynamics predicted for the CFO layer by two types of simulations.

As in the case of thick CFO films, the longitudinal elastic wave propagating in the CFO layer initially creates a spin wave with the same frequency and wavelength. The formed magnetoelastic wave reflects from the CFO|Pt interface and interferes with the incoming wave constantly generated by the piezoelectric transducer. After several reflections, the magnetoelastic dynamics in the CFO layer becomes rather complex. Nevertheless, a steady-state magnetization precession with constant frequency and amplitude sets in at the CFO|Pt interface after a transient regime lasting about 1 ns for the crystalline layer and 15 ns for the amorphous one [see Figs. 7(a) and 7(b)]. It should be noted that time dependences of the direction cosines  $m_i$  are almost sinusoidal in the crystalline layer at the chosen maximal strain  $\epsilon_{zz}^{\text{max}} = 5 \times 10^{-4}$  in the driving wave. In contrast, the dependences  $m_i(t)$  appear to be clearly nonsinusoidal in the amorphous CFO layer despite much smaller value of  $\epsilon_{zz}^{\text{max}} = 5 \times 10^{-5}$  used in the simulations in order to avoid strain-induced magnetization switching. This feature is due to the much larger solid angle  $\Omega$  of the magnetization precession in the amorphous CFO layer lacking strong magnetic anisotropy and being subjected to a weak magnetic field.

Magnetization precession at the CFO|Pt interface should lead to a spin pumping into the Pt layer, because such precession acts as a pump which transfers angular momentum from the ferromagnet to electrons in the normal metal that reflect from the interface [56]. The spin current density  $\mathbf{J}_s(z = t_F, t)$  at the interface can be calculated as

$$\mathbf{J}_s = \frac{\hbar}{4\pi} \text{Re}[g'_{\uparrow\downarrow}] \mathbf{m} \times \frac{d\mathbf{m}}{dt}, \quad (6)$$

since the real part of the reflection spin mixing conductance  $g'_{\uparrow\downarrow}$  per unit contact area dominates over the imaginary one, and the transmission spin mixing conductance  $g'_{\uparrow\downarrow}$  is absent in the case of insulator-metal contacts [57]. The product  $\mathbf{m} \times d\mathbf{m}/dt$  involved in Eq. (6) was evaluated using the dependence  $\mathbf{m}(z = t_F, t)$  provided by our micromagnetic simulations, which allow for the backaction of spin pumping on the magnetization dynamics by introducing the enhanced Gilbert damping [39,58] in the CFO computational cells adjacent to the interface. This enabled us to determine the spin current density  $\mathbf{J}_s(z = t_F, t)$  normalized by the factor  $\hbar/(4\pi)\text{Re}[g'_{\uparrow\downarrow}]$ . Figures 7(c) and 7(d) show that the oscillation amplitudes of all three projections of  $\mathbf{J}_s$  on the coordinate axes appear to be larger in the Pt layer contacting crystalline CFO film. However, the oscillations of these projections  $J_i^s$  in the bilayer comprising amorphous CFO film have the same order of magnitude. This result stems from the fact that relatively small frequency of magnetization precession in such film, which reduces the derivative  $d\mathbf{m}/dt$  involved in Eq. (6), is largely compensated for by much bigger precession amplitude. By filtering out the high-frequency oscillations of  $\mathbf{J}_s$  with the aid of the Savitzky-Golay algorithm, we determined the nonoscillating component  $\langle \mathbf{J}_s \rangle$  of the spin current. As seen from Figs. 7(e) and 7(f),  $\langle \mathbf{J}_s \rangle$  increases rapidly during a short transition period and then becomes constant, which enables us to consider it a dc component. The dc spin current has only two significant projections on the coordinate axes,

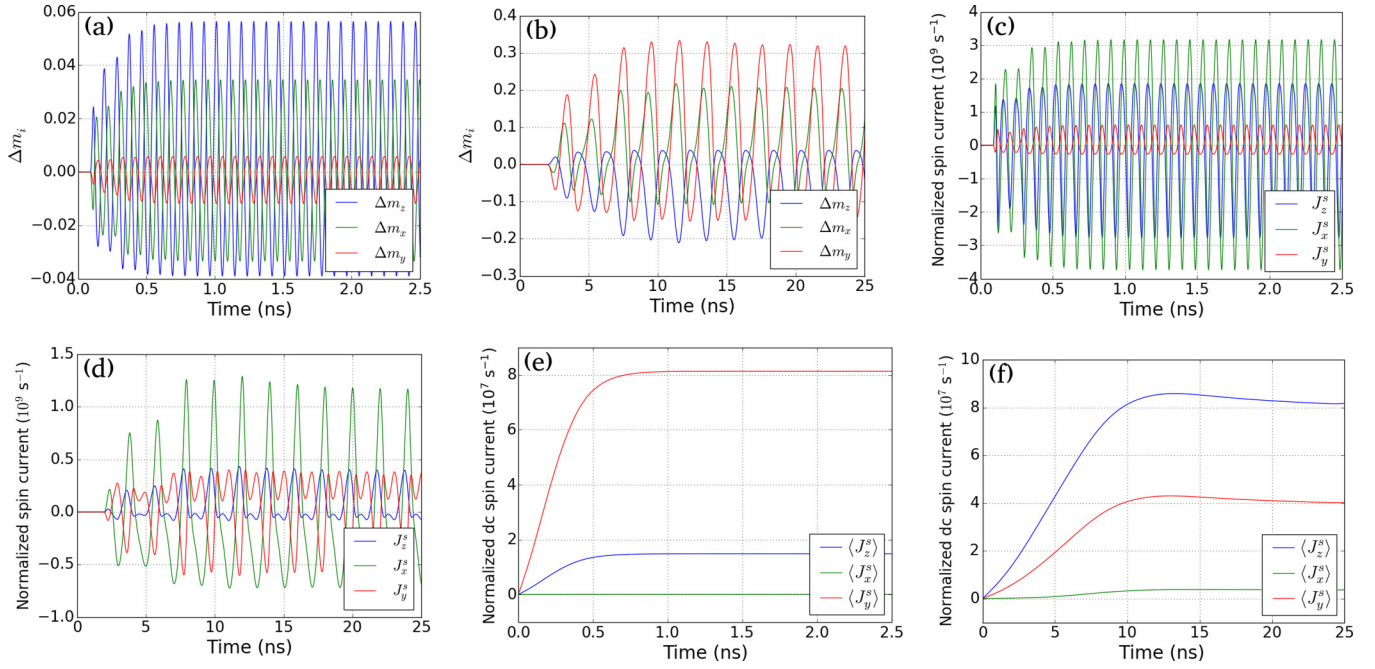


FIG. 7. Magnetization dynamics and spin pumping at CFO|Pt interface. Panels (a) and (b) show changes  $\Delta m_i(t)$  in the direction cosines of the oscillating magnetization in crystalline (at  $\nu = 11$  GHz) and amorphous (at  $\nu = 0.5$  GHz) CFO layers, respectively. Panels (c) and (d) present the time dependences of the spin current pumped into the Pt layer by crystalline and amorphous CFO layers. Panels (e) and (f) demonstrate the dc component of the pumped spin current for the bilayers comprising crystalline and amorphous CFO films, respectively. The spin-current densities  $J_i^s$  at the interface are normalized by the quantity  $\hbar/(4\pi)\text{Re}[g'_{\uparrow\downarrow}]$ .

$\langle J_y^s \rangle$  and  $\langle J_z^s \rangle$ , which have rather different magnitudes in Pt layers contacting crystalline and amorphous CFO films. Since  $\langle \mathbf{J}_s \rangle$  eventually assumes a constant value in the steady-state regime, the CFO/Pt heterostructure can be employed as an acoustically driven injector of both ac and dc spin currents.

Owing to spin relaxation and diffusion in Pt, the spin current density  $\langle \mathbf{J}_s \rangle$  decays with the distance  $z - t_F$  from the CFO|Pt interface according to the relation [59]

$$\langle \mathbf{J}_s(z) \rangle = \langle \mathbf{J}_s^0 \rangle \frac{\sinh\left(\frac{t_F + t_N - z}{\xi_{sd}}\right)}{\sinh\left(\frac{t_N}{\xi_{sd}}\right)}, \quad (7)$$

where  $\langle \mathbf{J}_s^0 \rangle$  denotes the value of  $\langle \mathbf{J}_s \rangle$  at  $z = t_F$ , and  $\xi_{sd} = 3.4$  nm is the spin diffusion length of Pt [60]. The nonuniform dc spin current gives rise to a dc charge current due to the inverse spin Hall effect (ISHE). The density  $\langle \mathbf{J}_c^{\text{ISHE}} \rangle$  of the corresponding charge current can be evaluated using the formula [59]

$$\langle \mathbf{J}_c^{\text{ISHE}} \rangle = \alpha_{\text{SH}} \frac{2e}{\hbar} \mathbf{e}_s \times \langle \mathbf{J}_s \rangle, \quad (8)$$

where  $\alpha_{\text{SH}} = 0.056$  is the spin Hall angle of Pt [60],  $e$  is the positive elementary charge, and  $\mathbf{e}_s$  is the unit vector in the direction of spin current, which is parallel to the  $z$  axis in our setting. Since  $\mathbf{e}_s$  is orthogonal to the CFO|Pt interface, the charge current  $\langle \mathbf{J}_c \rangle$  is expected to flow along the interface. Under open-circuit electrical boundary conditions, however, such flow should create a charge accumulation at the sides of the Pt layer, which generates an electric field  $\langle \mathbf{E} \rangle$  in Pt. Hence, the actual dc charge current  $\langle \mathbf{J}_c \rangle$  is the sum of the ISHE contribution given by Eq. (8) and the drift current  $\langle \mathbf{J}_c^{\text{drift}} \rangle = \sigma_N \langle \mathbf{E} \rangle$  depending on the conductivity  $\sigma_N$  of Pt.

It is important to evaluate the charge current  $\langle \mathbf{J}_c \rangle$  and the spatial distribution of time-averaged electric potential  $\langle \varphi \rangle$  in the Pt layer, because potential difference between the sides of the normal-metal layer can be used to detect the spin pumping experimentally [61]. Since the projection of  $\langle \mathbf{J}_s \rangle$  on the  $z$  axis does not create any charge current ( $\langle \mathbf{J}_c^{\text{ISHE}} \rangle$ ) and the projection  $\langle J_x^s \rangle$  is zero or very small [see Figs. 7(e) and 7(f)], the charge current  $\langle \mathbf{J}_c^{\text{ISHE}} \rangle$  is governed by the density  $\langle J_y^s \rangle$  and flows along the  $x$  axis. Hence, it is sufficient to calculate the two-dimensional distributions of  $\langle \mathbf{J}_c \rangle$  and  $\langle \varphi \rangle$  in the  $xz$  plane. To solve the problem, we used the Laplace's equation for the electric potential together with the appropriate boundary conditions  $\partial \langle \varphi \rangle / \partial z = 0$  (at  $z = t_F$  and  $z = t_F + t_N$ ) and  $\sigma_N \partial \langle \varphi \rangle / \partial x = \langle J_x^{\text{ISHE}} \rangle$  (at  $x = 0$  and  $x = w_N$ , where  $w_N$  is the width of the Pt layer). These boundary conditions follow from the fact that the projection of the total charge current  $\langle \mathbf{J}_c \rangle = \langle \mathbf{J}_c^{\text{ISHE}} \rangle + \langle \mathbf{J}_c^{\text{drift}} \rangle$  on the normal to the Pt surface should be zero at that surface. In the numerical calculations of  $\langle \varphi \rangle$ , we assumed the width  $w_N$  to be  $40 \mu\text{m}$  and employed the spin mixing conductance  $\text{Re}[g'_{\uparrow\downarrow}] = 0.62 \times 10^{19} \text{m}^{-2}$  determined experimentally for the CFO|Pt interface [62] and the measured conductivity  $\sigma_N = 9.35 \times 10^6 \text{S m}$  of Pt [44]. The obtained potential distribution  $\langle \varphi \rangle(x, z)$  enabled us to calculate the drift current  $\langle \mathbf{J}_c^{\text{drift}} \rangle = -\sigma_N \nabla \langle \varphi \rangle$  and the total dc current  $\langle \mathbf{J}_c \rangle$  in the Pt layer. The maps presented in Figs. 8(a) and 8(b) demonstrate that  $\langle \mathbf{J}_c \rangle$  forms a peculiar vortexlike pattern, which resembles the dynamics of a fluid put into motion at the interface. The magnitude of the current density  $\langle J_c \rangle$  assumes the largest value at the CFO|Pt interface, where it equals about  $6.75 \times 10^5$  and  $2.7 \times 10^5 \text{A m}^{-2}$  in the bilayers comprising crystalline and amorphous CFO films,

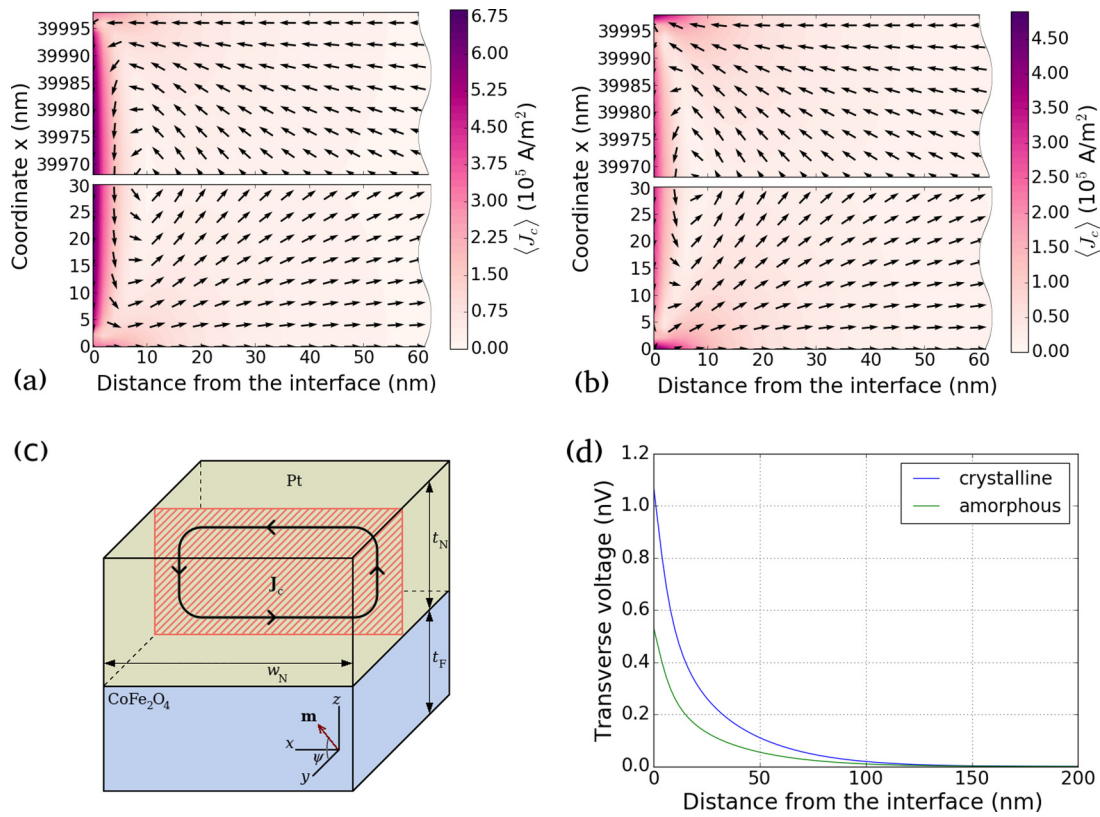


FIG. 8. Two-dimensional maps showing spatial distributions of the density of dc charge current, which flows in thick Pt films contacting crystalline (a) and amorphous (b) CFO layers. The magnitude of the charge current density is indicated by color, while the arrows show the direction of charge flow. The maps describe the 60-nm-thick region of the Pt layer near the interface with the CFO and lie in the hatched  $z$ - $x$  plane demonstrated in panel (c). Panel (d) shows the variations of the transverse dc voltage between the sides of the Pt layer with the distance from the interface with the crystalline/amorphous CFO layer. The thickness and width of the Pt film, which generally affect the charge current and transverse voltage, are taken to be  $t_N = 4\mu\text{m}$  and  $w_N = 40\mu\text{m}$ .

respectively, and falls rapidly with distance inside the normal metal. The corresponding transverse dc voltage  $\langle \Delta V \rangle = \langle \varphi \rangle(x = w_N, z) - \langle \varphi \rangle(x = 0, z)$  between the sides of the Pt layer is plotted as a function of the distance  $z - t_F$  from the interface in Fig. 8(d). Remarkably,  $\langle \Delta V \rangle$  has a value of about 1 nV at the interface with the crystalline CFO, which can be registered experimentally and further increased by using acoustic waves with larger maximal strains  $\epsilon_{zz}^{\text{max}}$  to excite the magnetization precession. Near the interface with the amorphous CFO,  $\langle \Delta V \rangle$  amounts to about 0.5 nV at the chosen small maximal strain  $\epsilon_{zz}^{\text{max}} = 5 \times 10^{-5}$ , which cannot be raised significantly because of the emergence of strain-induced magnetization switching. However, the amplitudes of alternating spin currents generated by both crystalline and amorphous CFO films are much larger than the dc spin currents created by them (see Fig. 7), which should result in much higher magnitudes of transverse ac voltages. Since the resonance frequency of the amorphous CFO layer is much lower than that of the crystalline one, such layers could be advantageous for applications in acoustically driven spin injectors requiring sub-GHz operating frequencies. The spin current generated in the Pt layer by the dynamically strained CFO film can be employed for the transfer of spin signals across metallic interlayers in spintronic circuits. Since the oscillating spin current creates an alternating charge current owing to the ISHE, the spin pumping into Pt could be also

employed for the generation of high-frequency electromagnetic fields.

## V. CONCLUSION

In this work, we performed an advanced computational analysis of coupled elastic and spin dynamics induced by longitudinal strain waves injected into crystalline and amorphous CFO films and CFO/Pt bilayers. We revealed that a monochromatic elastic wave, which can be generated by an attached piezoelectric transducer, selectively excites a spin wave with the same frequency and wavelength. The efficiency of strain-driven spin wave excitation maximizes when the frequency  $\nu$  of injected elastic wave matches the resonance frequency  $\nu_r$  of unstrained CFO film, but such excitation retains comparable efficiency in a rather wide range of frequencies around  $\nu_r$ . Owing to the magnetoelastic coupling between spins and strains, the driving longitudinal wave serves as a carrier for the spin wave and endows it with the elastic dispersion relation at all studied excitation frequencies. Remarkably, the formed magnetoelastic wave propagates over rather long distances in CFO despite its high Gilbert damping.

Our micromagnetic modeling also demonstrated the appearance of secondary elastic waves caused by the backaction of inhomogeneous magnetization precession on strain state of CFO. These transverse waves, which were not predicted by

previous simulations of the propagation of longitudinal waves along a Ni bar [28], have much smaller amplitudes than the driving elastic wave and peculiar profiles. The magnetoelastic feedback also lies at the origin of a noticeable decay revealed for the driving longitudinal elastic wave propagating in CFO. Fortunately, the decay length  $L_{\text{dec}}(\nu)$  characterizing such magnetically induced damping of the driving wave is rather large, amounting to about  $70 \mu\text{m}$  at  $\nu = \nu_r$ . It should be noted that the energy transfer from the strain wave traveling in CFO to the magnetic subsystem can be detected experimentally. To that end, it is sufficient to compare the attenuation of a high-frequency longitudinal wave at different orientations of the CFO magnetization  $\mathbf{M}$  with respect to wave vector  $\mathbf{k}_L$ . For instance, when  $\mathbf{k}_L$  is orthogonal to the surfaces of an in-plane magnetized CFO film, the magnetic damping appears only in the presence of an out-of-plane external magnetic field, which creates nonzero projection of  $\mathbf{M}$  on  $\mathbf{k}_L$  necessary for the generation of magnetization precession by the elastic wave.

For CFO/Pt bilayers, we found that the injected longitudinal wave generates a magnetization precession at the interface, which assumes a steady-state character after a short transition period. Our theoretical calculations showed that

such precession gives rise to a stable spin current flowing in Pt, which has both ac and dc components. Owing to the ISHE, the pumped spin current creates a vortexlike charge current in thick Pt layer under open-circuit boundary conditions, which generates a nonuniform distribution of the electric potential. Importantly, the voltage between lateral sides of the Pt layer may exceed 1 nV, which can be registered experimentally, pointing to significant efficiency of the elastically driven spin pumping.

Thus, the results obtained in this work indicate that CFO can be a promising material for the acoustic spintronics and magnonics. Prospective device applications of CFO films include elastically driven spin injectors with ultralow power consumption [31], logic gates using the phase of spin waves [63,64], and reconfigurable spin-based logic circuits [65]. We hope that our theoretical predictions will trigger experimental studies of strain-induced spin phenomena in CFO films and heterostructures.

#### ACKNOWLEDGMENT

This work was supported by the Foundation for the Advancement of Theoretical Physics and Mathematics BASIS.

- 
- [1] N. Akulov, *Z. Phys.* **52**, 389 (1928).  
 [2] C. Kittel, *Rev. Mod. Phys.* **21**, 541 (1949).  
 [3] A. V. Scherbakov, A. S. Salasyuk, A. V. Akimov, X. Liu, M. Bombeck, C. Brüggemann, D. R. Yakovlev, V. F. Sapega, J. K. Furdyna, and M. Bayer, *Phys. Rev. Lett.* **105**, 117204 (2010).  
 [4] L. Thevenard, E. Peronne, C. Gourdon, C. Testelin, M. Cubukcu, E. Charron, S. Vincent, A. Lemaître, and B. Perrin, *Phys. Rev. B* **82**, 104422 (2010).  
 [5] S. Davis, A. Baruth, and S. Adenwalla, *Appl. Phys. Lett.* **97**, 232507 (2010).  
 [6] M. Weiler, L. Dreher, C. Heeg, H. Huebl, R. Gross, M. S. Brandt, and S. T. B. Goennenwein, *Phys. Rev. Lett.* **106**, 117601 (2011).  
 [7] K. Uchida, H. Adachi, T. An, T. Ota, M. Toda, B. Hillebrands, S. Maekawa, and E. Saitoh, *Nat. Mater.* **10**, 737 (2011).  
 [8] K.-I. Uchida, T. An, Y. Kajiwara, M. Toda, and E. Saitoh, *Appl. Phys. Lett.* **99**, 212501 (2011).  
 [9] T. H. E. Lahtinen, K. J. A. Franke, and S. van Dijken, *Sci. Rep.* **2**, 258 (2012).  
 [10] M. Weiler, H. Huebl, F. S. Goerg, F. D. Czeschka, R. Gross, and S. T. B. Goennenwein, *Phys. Rev. Lett.* **108**, 176601 (2012).  
 [11] J.-W. Kim, M. Vomir, and J.-Y. Bigot, *Phys. Rev. Lett.* **109**, 166601 (2012).  
 [12] S. Cherepov, P. Khalili Amiri, J. G. Alzate, K. Wong, M. Lewis, P. Upadhyaya, J. Nath, M. Bao, A. Bur, T. Wu, G. P. Carman, A. Khitun, and K. L. Wang, *Appl. Phys. Lett.* **104**, 082403 (2014).  
 [13] L. Thevenard, C. Gourdon, J. Y. Prieur, H. J. von Bardeleben, S. Vincent, L. Becerra, L. Largeau, and J.-Y. Duquesne, *Phys. Rev. B* **90**, 094401 (2014).  
 [14] K. J. A. Franke, B. Van de Wiele, Y. Shirahata, S. J. Hämäläinen, T. Taniyama, and S. van Dijken, *Phys. Rev. X* **5**, 011010 (2015).  
 [15] J. Januonis, C. L. Chang, P. H. M. van Loosdrecht, and R. I. Tobey, *Appl. Phys. Lett.* **106**, 181601 (2015).  
 [16] P. G. Gowtham, T. Moriyama, D. C. Ralph, and R. A. Buhrman, *J. Appl. Phys.* **118**, 233910 (2015).  
 [17] V. Sampath, N. D'Souza, D. Bhattacharya, G. M. Atkinson, S. Bandyopadhyay, and J. Atulasimha, *Nano Lett.* **16**, 5681 (2016).  
 [18] Y. Hashimoto, D. Bossini, T. H. Johansen, E. Saitoh, A. Kirilyuk, and T. Rasing, *Phys. Rev. B* **97**, 140404(R) (2018).  
 [19] A. I. Akhiezer, V. G. Bariakhtar, and S. V. Peletminski, *Zh. Eksperim. i Teor. Fiz.* **35**, 228 (1958) [*Sov. Phys. JETP* **8**, 157 (1959)].  
 [20] C. Kittel, *Phys. Rev.* **110**, 836 (1958).  
 [21] L. Dreher, M. Weiler, M. Pernpeintner, H. Huebl, R. Gross, M. S. Brandt, and S. T. B. Goennenwein, *Phys. Rev. B* **86**, 134415 (2012).  
 [22] A. Kamra, H. Keshtgar, P. Yan, and G. E. W. Bauer, *Phys. Rev. B* **91**, 104409 (2015).  
 [23] N. I. Polzikova, S. G. Alekseev, V. A. Luzanov, and A. O. Raevskiy, *Phys. Solid State* **60**, 2211 (2018).  
 [24] J. Dean, M. T. Bryan, G. Hrkac, A. Goncharov, C. L. Freeman, M. A. Bashir, T. Schreffl, and D. A. Allwood, *J. Appl. Phys.* **108**, 073903 (2010).  
 [25] C.-Y. Liang, S. M. Keller, A. E. Sepulveda, A. Bur, W.-Y. Sun, K. Wetzlar, and G. P. Carman, *Nanotechnology* **25**, 435701 (2014).  
 [26] J. Dean, M. T. Bryan, J. D. Cooper, A. Virbule, J. E. Cunningham, and T. J. Hayward, *Appl. Phys. Lett.* **107**, 142405 (2015).  
 [27] A. V. Azovtsev and N. A. Pertsev, *Phys. Rev. B* **94**, 184401 (2016).  
 [28] C. Chen, A. Barra, A. Mal, G. Carman, and A. Sepulveda, *Appl. Phys. Lett.* **110**, 072401 (2017).  
 [29] T. Mathurin, S. Giordano, Y. Dusch, N. Tiercelin, P. Pernod, and V. Preobrazhensky, *Phys. Rev. B* **95**, 140405(R) (2017).

- [30] R.-C. Peng, J.-M. Hu, L.-Q. Chen, and C.-W. Nan, *NPG Asia Mater.* **9**, e404 (2017).
- [31] A. V. Azovtsev and N. A. Pertsev, *Appl. Phys. Lett.* **111**, 222403 (2017).
- [32] X. Li, D. Labanowski, S. Salahuddin, and C. S. Lynch, *J. Appl. Phys.* **122**, 043904 (2017).
- [33] V. J. Folen, *Group III. Crystal and Solid State Physics. Vol. 4. Magnetic and Other Properties of Oxides and Related Compounds, Part B*, edited by K.-H. Hellwege and A. M. Hellwege, Landolt-Börnstein. Numerical Data and Functional Relationships in Science and Technology (Springer-Verlag, Berlin, 1970).
- [34] E. L. Verde, G. T. Landi, M. S. Carrio, A. L. Drummond, J. A. Gomes, E. D. Vieira, M. H. Sousa, and A. F. Bakuzis, *AIP Adv.* **2**, 032120 (2012).
- [35] Following a convention based on the general definition of waves and adopted in the recent papers [16,27,28,31,32], we use the term “spin waves” for strain-driven nonuniform magnetization oscillations generated by elastic waves. Although such forced spin waves generally do not satisfy the dispersion relation of classical spin waves, they also carry spin signals, which enables their use for information encoding in magnon spintronics.
- [36] A. Vansteenkiste, J. Leliaert, M. Dvornik, M. Helsen, F. Garcia-Sanchez, and B. Van Waeyenberge, *AIP Adv.* **4**, 107133 (2014).
- [37] V. A. M. Brabers, in *Handbook of Magnetic Materials*, edited by K. H. J. Buschow (Elsevier, Amsterdam, 1995), Vol. 8.
- [38] S. R. Pollack and K. R. Atkins, *Phys. Rev.* **125**, 1248 (1962).
- [39] Y. Tserkovnyak, A. Brataas, and G. E. W. Bauer, *Phys. Rev. Lett.* **88**, 117601 (2002).
- [40] J. Smit and H. P. J. Wijn, *Ferrites. Physical Properties of Ferrimagnetic Oxides in Relation to Their Technical Applications* (Philips Research Laboratories, Eindhoven, Netherlands, 1959).
- [41] H. C. Teh, M. F. Collins, and H. A. Mook, *Can. J. Phys.* **52**, 396 (1974).
- [42] M. S. N. Hiratsuka, *IEEE Trans. Magn.* **23**, 3326 (1987).
- [43] Z. Li, E. S. Fisher, J. Z. Liu, and M. V. Nevitt, *J. Mater. Sci.* **26**, 2621 (1991).
- [44] W. M. Haynes, *CRC Handbook of Chemistry and Physics*, 96th ed. (CRC Press, Boca Raton, FL, 2016).
- [45] D. N. Blaschke, *J. Appl. Phys.* **122**, 145110 (2017).
- [46] D. Jiles, *Introduction to Magnetism and Magnetic Materials* (Springer, New York, 1991).
- [47] H. F. Tiersten, *Linear Piezoelectric Plate Vibrations* (Springer Science+ Business Media, New York, 1969).
- [48] Edited by A. Safari and E. K. Akdogan, *Piezoelectric and Acoustic Materials for Transducer Applications* (Springer, Berlin, 2008).
- [49] V. V. Lemanov, A. V. Pavlenko, and A. N. Grishmanovski, J. Exptl. Theoret. Phys. (U.S.S.R.) **59**, 712 (1970) [Sov. Phys. JETP **32**, 389 (1971)].
- [50] H.-Y. Hao and H. J. Maris, *Phys. Rev. Lett.* **84**, 5556 (2000).
- [51] H.-Y. Hao and H. J. Maris, *Phys. Rev. B* **64**, 064302 (2001).
- [52] O. B. Wright and K. Kawashima, *Phys. Rev. Lett.* **69**, 1668 (1992).
- [53] A. V. Azovtsev and N. A. Pertsev, *Phys. Rev. Appl.* **10**, 044041 (2018).
- [54] A. E. Clark, B. DeSavage, W. Coleman, E. R. Callen, and H. B. Callen, *J. Appl. Phys.* **34**, 1296 (1963).
- [55] C. Liu, J. Chen, T. Liu, F. Heimbach, H. Yu, Y. Xiao, J. Hu, M. Liu, H. Chang, T. Stueckler, S. Tu, Y. Zhang, Y. Zhang, P. Gao, Z. Liao, D. Yu, K. Xia, N. Lei, W. Zhao, and M. Wu, *Nat. Commun.* **9**, 738 (2018).
- [56] Y. Tserkovnyak, A. Brataas, G. E. W. Bauer, and B. I. Halperin, *Rev. Mod. Phys.* **77**, 1375 (2005).
- [57] X. Jia, K. Liu, K. Xia, and G. E. W. Bauer, *Europhys. Lett.* **96**, 17005 (2011).
- [58] A. Kapelrud and A. Brataas, *Phys. Rev. Lett.* **111**, 097602 (2013).
- [59] O. Mosendz, J. E. Pearson, F. Y. Fradin, G. E. W. Bauer, S. D. Bader, and A. Hoffmann, *Phys. Rev. Lett.* **104**, 046601 (2010).
- [60] J.-C. Rojas-Sánchez, N. Reyren, P. Laczkowski, W. Savero, J.-P. Attané, C. Deranlot, M. Jamet, J.-M. George, L. Vila, and H. Jaffrès, *Phys. Rev. Lett.* **112**, 106602 (2014).
- [61] E. Saitoh, M. Ueda, H. Miyajima, and G. Tatara, *Appl. Phys. Lett.* **88**, 182509 (2006).
- [62] M. Isasa, A. Bedoya-Pinto, S. Vlez, F. Golmar, F. Sanchez, L. E. Hueso, J. Fontcuberta, and F. Casanova, *Appl. Phys. Lett.* **105**, 142402 (2014).
- [63] M. P. Kostylev, A. A. Serga, T. Schneider, B. Leven, and B. Hillebrands, *Appl. Phys. Lett.* **87**, 153501 (2005).
- [64] T. Schneider, A. A. Serga, B. Leven, B. Hillebrands, R. L. Stamps, and M. P. Kostylev, *Appl. Phys. Lett.* **92**, 022505 (2008).
- [65] A. Khitun, M. Bao, and K. L. Wang, *IEEE Trans. Magn.* **44**, 2141 (2008).